AI Applications for Disease Diagnosis and Treatment

Rajae El Ouazzani
Moulay Ismail University of Meknes, Morocco

Mohammed Fattah
Moulay Ismail University of Meknes, Morocco

Nabil Benamar
Moulay Ismail University of Meknes, Morocco

A volume in the Advances in Medical Diagnosis, Treatment, and Care (AMDTC) Book Series

IGI Global
PUBLISHER of TIMELY KNOWLEDGE

Published in the United States of America by
IGI Global
Medical Information Science Reference (an imprint of IGI Global)
701 E. Chocolate Avenue
Hershey PA, USA 17033
Tel: 717-533-8845
Fax: 717-533-8661
E-mail: cust@igi-global.com
Web site: http://www.igi-global.com

Library of Congress Cataloging-in-Publication Data

Names: El Ouazzani, Rajae, 1981- editor. | Fattah, Mohammed, 1982- editor. | Benamar, Nabil, 1973- editor.
Title: AI applications for disease diagnosis and treatment / Rajae El Ouazzani, Mohammed Fattah, and Nabil Benamar, editors.
Description: Hershey, PA : Engineering Science Reference, [2022] | Includes bibliographical references and index. | Summary: “This book studies the application of AI tools on healthcare such as machine learning, deep learning, soft computing, and evolutionary computing techniques in the design, and implementation of healthcare solutions, exploring many healthcare research topics such as disease diagnosis and assistance, diet proposal, physical and psychological assistance, and drug prescription and trucking”-- Provided by publisher.
Identifiers: LCCN 2021061497 (print) | LCCN 2021061498 (ebook) | ISBN 9781668423042 (hardcover) | ISBN 9781668423059 (paperback) | ISBN 9781668423066 (ebook)
Subjects: LCSH: Artificial intelligence--Medical applications. | Machine learning. | Medical informatics.
Classification: LCC R859.7.A78 A395 2022 (print) | LCC R859.7.A78 (ebook) | DDC 610.285--dc23/eng/20211216
LC record available at https://lccn.loc.gov/2021061497
LC ebook record available at https://lccn.loc.gov/2021061498

This book is published in the IGI Global book series Advances in Medical Diagnosis, Treatment, and Care (AMDTC) (ISSN: 2475-6628; eISSN: 2475-6636)

British Cataloguing in Publication Data
A Cataloguing in Publication record for this book is available from the British Library.

Editorial Advisory Board

Table of Contents

Chapter 4
Fully Automatic Epiretinal Membrane Segmentation in OCT Scans Using Convolutional Networks

Mateo Gende
CITIC, INIBIC, Universidade da Coruña, Spain

Joaquim de Moura
https://orcid.org/0000-0002-2050-3786
CITIC, INIBIC, Universidade da Coruña, Spain

Jorge Novo
CITIC, INIBIC, Universidade da Coruña, Spain

Marcos Ortega
CITIC, INIBIC, Universidade da Coruña, Spain

ABSTRACT

The epiretinal membrane (ERM) is an ocular pathology that can cause visual distortions. To prevent a loss of vision, symptomatic ERM needs to be removed before it can cause irreversible damage. In order to do this, the ERM needs to be located early, so that it can be peeled from the retina. This chapter explores an automatic methodology for ERM segmentation, as well as its intuitive visualization in the form of colour maps. To do this, visual features that are compatible with ERM presence are extracted from ophthalmologic images by using computer vision algorithms and deep learning models. This methodology achieved satisfactory results, reaching a dice coefficient of 0.826 and a Jaccard index of 0.714, contributing to highlight the applicability of deep learning models for the detection of pathological signs in medical images.

DOI: 10.4018/978-1-6684-2304-2.ch004

INTRODUCTION

Thanks to recent advances in computation architectures and in the development of new and improved artificial intelligence algorithms, Computer-aided Diagnosis (CAD) systems are becoming increasingly relevant in healthcare services, finding application in fields such as audiometry (Fernández, et al., 2018), radiology (Romeny et al., 1998) or encephalography (Hosny et al., 2018). Among the different domains of application of CAD systems, the analysis of medical images stands out.

Deep learning is a subset of machine learning focused on the development of artificial neural network models that have multiple layers in order to progressively extract higher-level features from data (LeCun et al., 2015). Convolutional neural networks are artificial neural networks that use the convolution operation in order to be able to extract visual features from images (Lecun et al., 1998). Thanks to the advent of deep convolutional neural networks, deep learning models are nowadays used for several tasks in the field of image analysis. These tasks can range from image classification (Krizhevsky et al., 2017), in which images are separated in classes according to their content; to image segmentation (Long et al., 2015), where images are partitioned into multiple segments, or every pixel in their content is labelled; to regression (Lv et al., 2014), where a value or a set of values are extracted from the images. With a focus on healthcare, deep convolutional neural networks have successfully been used to analyze and study anatomical structures as well as pathological signs in medical images of several types (Shen et al., 2017; Litjens et al., 2017). In particular, deep learning-based CAD systems have found uses in medical imaging techniques such as magnetic resonance imaging (Kamnitsas et al., 2017), conventional radiography (Lakhani & Sundaram, 2017), ultrasound (Cheng et al., 2016) or computed tomography scans (Setio et al., 2016). These systems have demonstrated that their performance can be on par with, or even exceed that of human experts in different diagnosis-related tasks (Litjens et al., 2017; Lee et al., 2020; Ting et al., 2017; Gulshan et al., 2016).

In ophthalmology, Optical Coherence Tomography (OCT) is an imaging technique that allows the in-depth visualization of tissue (Huang et al., 1991). By shining a beam of low coherence (high bandwidth) light over the tissue and measuring the differences in phase and amplitude in the reflected beam compared to a reference one, a one-dimensional reading or A-Scan can be acquired at every scanned spot. This A-Scan contains depth-wise information about the reflectivity of the scanned tissue. If this beam is swept through the surface of the tissue, these readings can be combined into a two-dimensional reading or B-Scan (Figure 1). These B-Scans can be visualized as high-resolution images which show a cross-sectional view of the tissue, like a tomogram containing the histological information of the scanned tissue. Furthermore, these B-Scans can be laterally combined to produce a volumetric

representation of the underlying tissue. This makes OCT a remarkably useful technique for the analysis of healthy or pathological ocular structures since these volumes allow the complete histological visualisation of the retinal tissue *in vivo* and in a non-invasive manner. For reference, OCT images can be used for the study of the vascular structure of the eye (Kashani et al., 2017; de Moura et al., 2016, 2017a; Spaide et al., 2018); for the diagnosis of glaucoma (Hood, 2017) (Tan et al., 2009; Jaffe & Caprioli, 2004), which is the most common cause of blindness in the developed world for people over 50; exudative macular disease (de Moura et al., 2017b), one of the most common causes of blindness in the developed world; or that of diabetic macular oedema (Hee, 1995; de Moura et al., 2019, 2020; Mookiah et al., 2013), the leading cause of blindness in patients of diabetes mellitus.

Figure 1. Example of an OCT slice or B-Scan, illustrated over an eye fundus image showcasing its location

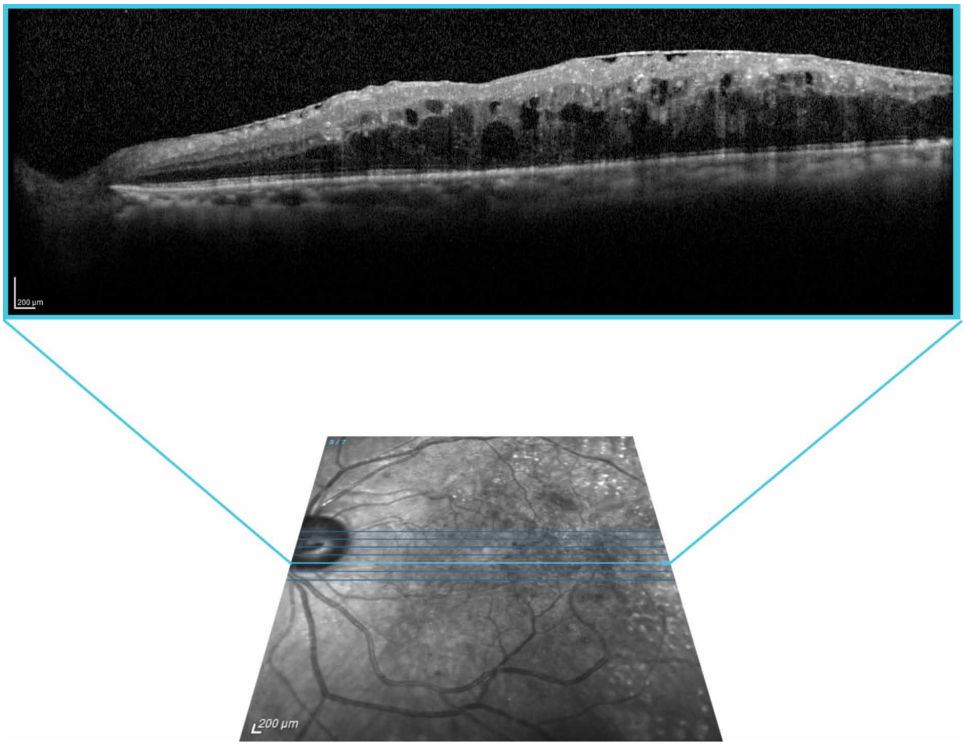

This chapter explores a methodology developed for the automatic detection and segmentation of one such ocular pathology, the Epiretinal Membrane (ERM). The ERM is a thin fibrocellular sheet that may appear over the retina surface. This layer

is mostly transparent and can be imagined as a thin film of cellophane stuck to the fundus of the eye. It is known by different names such as cellophane maculopathy, macular pucker, macular fibrosis, or surface wrinkling retinopathy. These names reference the effects that this layer can have over the tissue of the retina. While it is mostly transparent and may not cause any symptoms, the ERM may also start to harden and contract after appearing. This causes mechanical traction over the underlying tissue, which in turn may start to deform and wrinkle the retina. The ERM is typically formed over the boundary between the vitreous body and the retina tissue, this area is known as the Inner Limiting Membrane (ILM). If the ERM is positioned over the retinal macula, these deformations may cause metamorphopsia (Matsumoto et al., 2003), a visual distortion that can manifest itself as a bowing in the centre of the visual field. For example, when observing parallel lines such as in an Amsler grid, these may appear to bow and bend to a patient suffering from metamorphopsia (Figure 2). Additionally, the deformations provoked by the ERM can also cause a thickening of the macular tissue, and in severe cases, the disappearance of the foveal pit. Although it is normally idiopathic, the ERM can also appear as a secondary factor to other related ocular pathologies. Diabetic macular oedema has a high prevalence of related ERM, with studies reporting that between 27 and 34% of oedema patients present ERM (Yamamoto et al., 2001; Ghazi et al.,2007). It can also appear as a response to external trauma to the eye, as a response to surgery or as a posterior complication of vitreous detachment or macular hole, among others. Generally, its appearance is caused by the retraction of the vitreous gel from the macula.

Figure 2. Example of the visual distortions that the metamorphopsia may cause to patients suffering from ERM over an Amsler grid

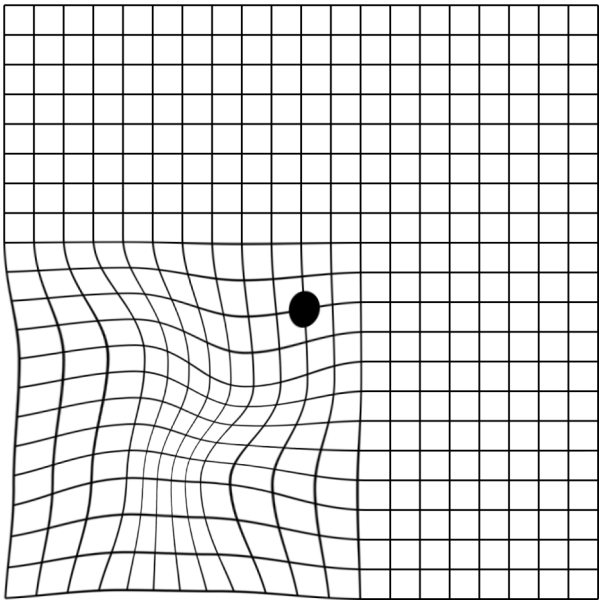

If the ERM is allowed to contract and deform the retina for long, some of the deformations it produces may become permanent. Treatment for symptomatic ERM involves a surgery known as *pars plana* vitrectomy (Suh et al., 2009), where a series of instruments are used to scrape the surface of the retina and peel away the fibrocellular layer. This surgery has higher chances of preserving the vision of the patients if performed early, before the exerted traction can further deform the tissue (Massin et al., 2000; Rahman & Stephenson, 2014), and it requires that the expert determines the extent and location of the ERM. This underscores the relevance of an early and accurate diagnosis of the ERM. Due to its transparency, the ERM is difficult to detect in eye fundus images (Figure 3). Often, only the deformations the ERM causes over the retina are visible in this imaging technique, and even then, only those that are very prominent. In OCT images, however, the ERM appears as a bright layer over the ILM (Figure 4). This imaging modality makes it much easier for the experts to detect and diagnose the ERM, as its high reflectivity facilitates its visualisation. Because of this, ERM diagnosis is usually performed by experts visually inspecting OCT images.

Figure 3. Example of a case of symptomatic ERM in an eye fundus image. Small creases over the tissue can be observed in the highlighted area

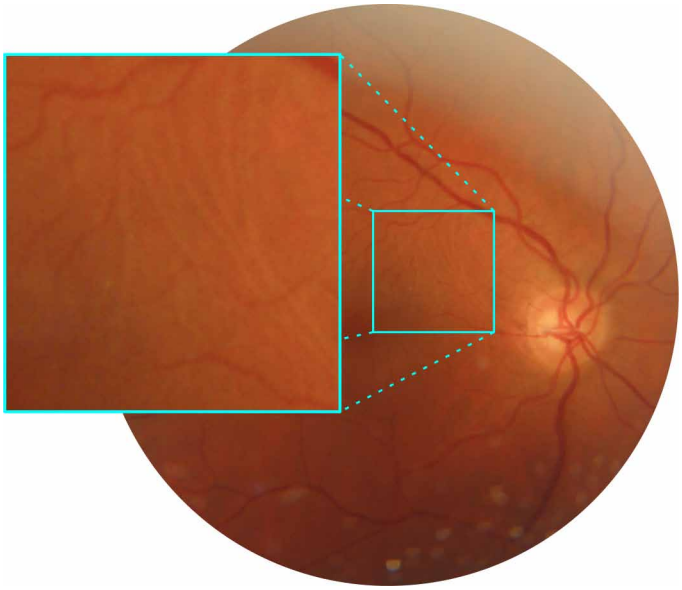

While the ERM is easier to detect in OCT slices, the visual inspection of images with the intention of screening for ERM signs is a time-consuming and inherently subjective process. Furthermore, the ERM is not the only reflective surface that can appear in OCT images, since visual artefacts caused by the forwards and backwards scattering of light can produce noise and bright spots in this image modality, making the visual detection of the ERM in OCT a non-trivial task.

Figure 4. OCT slice displaying the ERM and ERM-related lesions

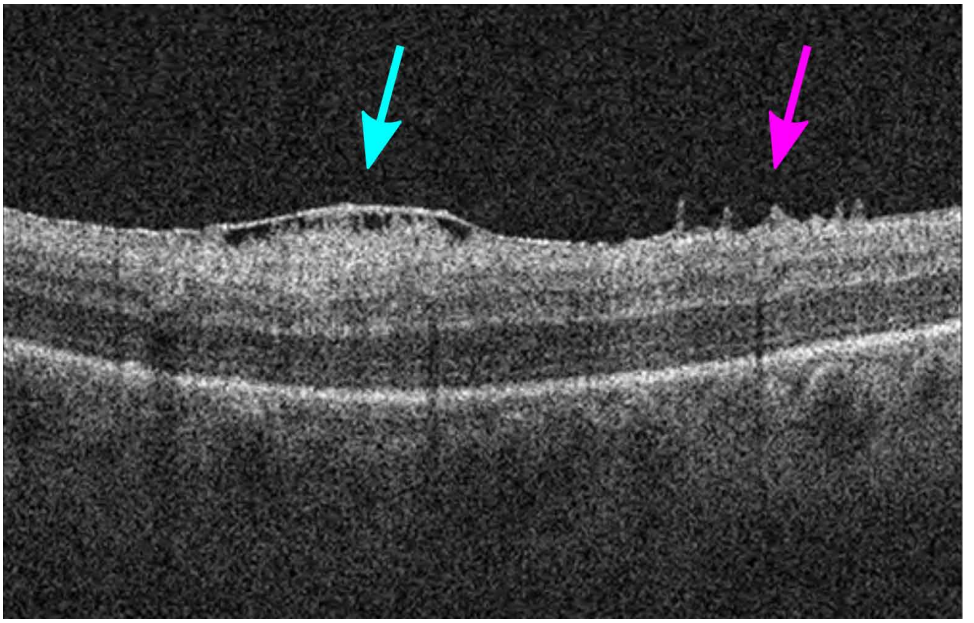

In this chapter, a methodology developed for the automatic segmentation of the ERM in OCT images is explored. The aim of this methodology is to provide the experts with an intuitive visualisation of the ERM presence (or lack thereof) in OCT volumes. To do this, the methodology consists of a series of three steps aimed at the preliminary detection of our Region of Interest (ROI), the segmentation of the ERM and, finally, the generation of intuitive segmentation maps that display the ERM overlaid on a reconstruction of the eye fundus, generated based on the original OCT volumes. These maps are also post-processed to incorporate cross-slice information into the segmentation results, helping minimise the stochastic errors that may be produced by the visual artefacts that are present in OCT images. The complete methodology makes use of different computer vision techniques, as well as deep learning algorithms in order to extract and analyse visual features which are relevant for the detection and diagnosis of the ERM. Moreover, thanks to the use of machine learning models, the segmentation process can be trained directly from annotated images, implicitly learning which visual features are relevant for the task at hand. This greatly simplifies the development process of CAD systems making use of this methodology.

The layout of this chapter is as follows: The Background section introduces how other works in the literature have approached the problem of the diagnosis of this pathology. The Epiretinal Membrane Segmentation section explains how each

of the steps that comprise this methodology are performed, the data that was used for its development, the deep learning model training details and the results that were obtained from evaluating the methodology. Solutions and Recommendations covers some of the solutions that were designed for the issues that arose during the development of this methodology. Future Research Directions indicates the different approaches that may be taken to further advance in the detection of this pathology. Finally, in Conclusion, the main ideas exposed in this chapter are summed up.

BACKGROUND

Due to the relevance of a disease such as the ERM, various works have addressed the challenge presented by its detection as an opportunity for the application of CAD systems that can aid in its diagnosis. This section shares an overview of how different works in the literature have approached the problem of detecting the ERM in medical imaging, a brief description of each one, as well as a summary of the advantages they may provide to the field of study and the shortcomings they might suffer from.

In the beginning, works such as the proposal by Wilkins *et al.* (1996) offered semi-automatic approaches for ERM diagnosis. These, however, relied on an initial manual annotation made by the expert indicating the location of the ERM in order to measure the macular thickening that it caused and assess the ERM.

Later works have introduced automatic methods, aiming to overcome the reliance on an initial expert annotation. As reference, Lu *et al.* (2018) used deep learning models for the detection of different pathologies, the ERM being one of them. A convolutional neural network was trained to classify images according to which of the four considered pathologies was present. The results obtained by this convolutional model were compared to those produced by two experts on the same task. These results showed that the system achieved a performance that was competitive with or better than that of human experts. In the work by Fang *et al.* (2017), the authors propose the detection of multiple macular lesions in OCT images. Among these lesions, the ERM was also considered. In order to perform this detection, a conventional feature extraction process was performed in segmented regions of interest. Using a machine learning-based system, these regions were then classified into the different macular lesions. Kuwayama *et al.* (2019) also proposed a system based on the classification of OCT slices. In a similar manner to the work by Lu *et al.*, the authors used a convolutional neural network for the classification into four different pathologies, achieving competitive results.

Sonobe *et al.* (2018) presented a study in which they compare the performance of support vector machines and deep learning models at detecting ERM cases in OCT

volumes. Images from the surface of the eye fundus, obtained from the software provided by the OCT scanner were used as input and a classification was performed by making use of the two proposed approaches. The results achieved by the deep learning model were higher than those obtained by the support vector machine approach. More recently, Lo *et al.* (2020) used a residual neural network architecture to screen for ERM in OCT images. Non-retinal specialised ophthalmologists were asked to participate in a test where their results were compared to those achieved by the residual neural network. In this comparison, the deep learning models performed slightly better than the ophthalmologists. More recently, Parra-Mora *et al.* (2021) described the use of four Deep learning-based classification architectures for the screening of the ERM. In the results, the authors claim a high discriminative performance by the deep learning models at classifying between OCT slices that displayed healthy eyes and slices showing ERM presence.

The results that were obtained in these works collectively show the potential that deep learning models possess for the screening of the ERM. These models have been proven to achieve a performance that can be on par with human experts and, in some cases, even exceed that of certified specialists. Additionally, comparisons between classical machine learning-based approaches that use conventional feature extraction and selection and deep learning models have shown that the latter may have the upper hand in terms of results. All of the previously mentioned approaches are based on the classification of OCT slices into whether they show healthy tissue or if signs compatible with the ERM are visible in the images. Furthermore, many of these proposals are focused on the screening of several pathologies, the ERM just being one of those considered and hardly the main focal point of these works.

Conversely, the works by Baamonde *et al.* (2017a, 2017b, 2019a) showcase a series of methods for the characterization of the ERM tissue in OCT images. These studies are completely focused on the detection of this pathology by means of different approaches such as local luminosity patterns or hand-crafted visual features. Moreover, in (Baamonde, et al., 2019b), the authors present the first approach for the segmentation of the ERM. This segmentation is done by means of the classification of patches. From every patch, the authors extracted a set of 452 conventional visual features, grey-level co-occurrence matrices, Gabor features, local binary patterns, Laws features) to intensity-based (intensity global features, grey-level intensity histograms, histograms of oriented gradients), as well as a set of domain-specific hand-crafted features. From this set of original features, the authors used the Spatial Uniform ReliefF algorithm to select the ones that contributed the most to the classification process. Finally, they provide a comparison between using random forests, k-nearest neighbours, and support vector machines for the classifications of different sets of selected features.

In this chapter, a refinement of the ERM segmentation methodology proposed by Baamonde *et al.* is explained (Gende et al., 2021). This methodology is refined by incorporating deep learning models into the classification process and providing an intuitive visualisation of the diseased tissue over a projection of the eye fundus.

EPIRETINAL MEMBRANE SEGMENTATION

This section explains the step-by-step process in which the presented methodology for the ERM segmentation in OCT images is subdivided. A visual summary of this methodology can be found in Figure 5. As previously mentioned, this segmentation methodology consists of a set of three steps, namely: the segmentation of the ROI, the classification of image patches and the final reconstruction of the intuitive representation. These will be explained in detail in the following subsections, as well as the data that was used to develop and test this methodology and the details of the neural network model training process.

Figure 5. Graphical summary of the methodology that is explored in this chapter. The original OCT volume is first subdivided into 2-dimensional B-Scans. Then, the ROI is segmented, and a series of windows centred on the ILM are extracted. These windows are classified by a convolutional neural network. Based on this classification, the segmentation map is reconstructed and postprocessed. A reconstruction of the eye fundus can be generated from the OCT volume. In parallel, this reconstruction and the segmentation map are overlaid to create the intuitive visualisation of ERM presence over the eye fundus.

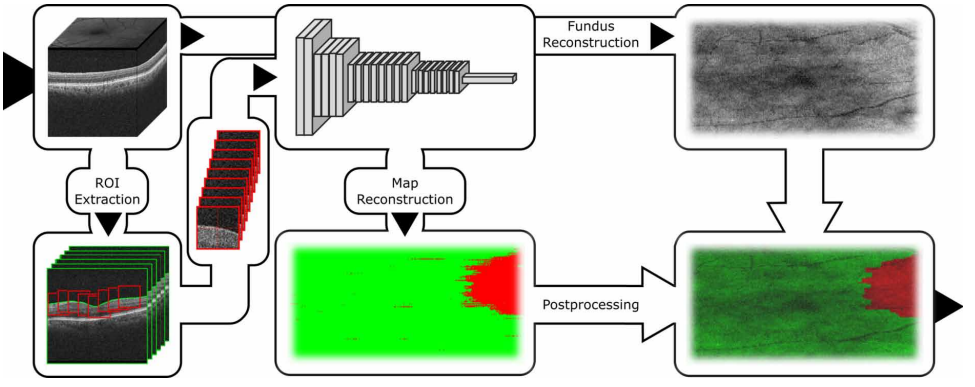

Region of Interest Segmentation

The first step is to segment the ROI location. In order to narrow down the area in which to look for the ERM, the boundary in which the ERM may appear if present must first be detected. This region is known as the Inner Limiting Membrane. Fortunately, due to the transparency of the vitreous body, the ILM is easy to detect in OCT slices. In these images, the retinal tissue is visible as are its internal structures, while the vitreous body appears as a slightly noisy background. This conveniently simplifies the task of detecting the position of the ILM.

Since the ILM appears as a continuous horizontal layer in these images, its position can be modelled as a height value. That is, for every image column in any OCT slice, there will be a pixel in which the ILM will begin. Thanks to this continuity, it is possible to convert this segmentation problem into a problem of determining the height of the ILM in every image column, which is much simpler.

To take advantage of the contrast that the ILM possesses in OCT images and the fact that the ILM can be modelled as a height value for every vertical column of pixels, active contour models can be used to segment the ROI (Gawlik et al., 2018). Active contour models, or snakes, are a computer vision framework used for determining the outlines of objects in images. One of the advantages of this framework is its robustness to noise. An active contour model can be defined as a set of n points v_i for i=0,…,n–1. The contour model is moderated by a set of two energies: $E_{external}$, the external energy which pulls the contour outwards toward the edges that are visible in the image and $E_{internal}$, the internal energy which elastically contracts the contour in order to preserve a smooth curve. Thus, the energy function of the snake can be described by Equation 1.

$$E^*_{snake} = \int_0^1 E_{snake}\left(\boldsymbol{v}(s)\right) ds = \int_0^1 E_{internal}\left(\boldsymbol{v}(s)\right) + E_{external}\left(\boldsymbol{v}(s)\right) ds \tag{1}$$

$E_{external}$ draws the snake towards visible edges in the image. It measures how well the curve matches image data. it can be described by Equation 2:

$$E_{external}(v) = -|G_y(v)|^2 \tag{2}$$

where G_y is the gradient in the y-axis. This makes it so that the active contour adjusts itself to edges in the image. Since the ILM describes an approximately horizontal line, only those pixels that possess the highest gradient in the y-axis are of interest.

On the other hand, $E_{internal}$ (Equation 3) reflects curve tension and curvature. Minimising the internal energy favours smooth, continuous curves.

$$E_{internal}(\boldsymbol{v}) = E_{continuity}(\boldsymbol{v}) + E_{curvature}(\boldsymbol{v})$$
$$E_{continuity}(\boldsymbol{v}) = \frac{1}{2}\left(\alpha(s)\left|\boldsymbol{v}_s(s)\right|^2\right) = \frac{1}{2}\left(\alpha(s)\left\|\frac{\partial \overline{\boldsymbol{v}}}{\partial s}(s)\right\|^2\right) \tag{3}$$
$$E_{curvature}(\boldsymbol{v}) = \frac{1}{2}\left(\beta(s)\left|\boldsymbol{v}_{ss}(s)\right|^2\right) = \frac{1}{2}\left(\beta(s)\left\|\frac{\partial^2 \overline{\boldsymbol{v}}}{\partial s^2}(s)\right\|^2\right)$$

where α(s) and β(s) are weights which control the sensitivity of the internal energy. α(s) penalises the separation between points in the contour. β(s) penalises oscillations between the positions of consecutive points, preserving curve smoothness.

OCT images generally present speckle noise due to the effects of light back-scattering (Samagaio et al., 2017). This noise can cause the active contours to fixate on bright spots that don't correspond to the real ILM location. In order to get rid of this noise, each original OCT slice is first pre-processed using a median filter. This filter assigns the median of the surrounding neighbours to each pixel. This way, the effects of isolated bright pixels can be minimised. To obtain the horizontal filters, a convolution using a y-axis Sobel filter is applied. This pre-processing stage can be visualised in Figure 6.

Figure 6. Initial pre-processing of an OCT slice prior to ILM segmentation. The image is filtered in order to remove noise and a Sobel operator in the y-axis is applied. This way the ILM can be highlighted over the fundus.

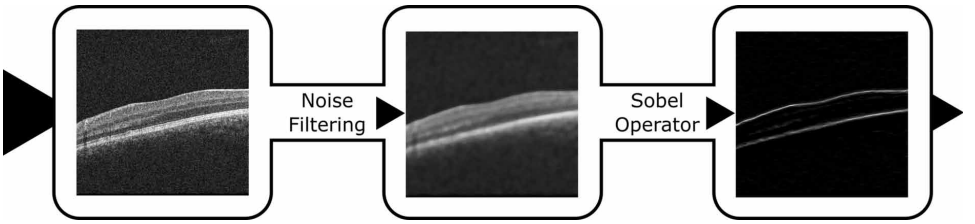

Once an image highlighting the horizontal edges in the original OCT slice has been obtained, the active contour can be adjusted. As previously indicated, since only the horizontal edge of the ILM is of relevance for this task, the active contour is initialised to the top of the image, with a contour point for every image column. These are allowed to iteratively move in the vertical axis, minimising the aforementioned internal and external energies until convergence. Once the active contour has settled over the ILM surface, its vertical position for every image column can be obtained,

effectively producing the segmentation of this layer. At this point, to proceed with the segmentation of the ERM, each ILM pixel will have to be classified into whether it is positioned over healthy or diseased tissue. Since a single pixel does not contain sufficient information about whether the tissue point it displays is diseased or not, a standard image window must first be extracted around each of these pixels. These windows contain the visual information surrounding the ILM pixel that is necessary for its correct classification. A summary of this process of window extraction can be visualised in Figure 7.

Figure 7. ILM segmentation. The active contour is allowed to contract downward until it converges on the ILM surface. Once the position of the ILM is determined, a window is extracted around each ILM pixel. These are to be classified on the next step.

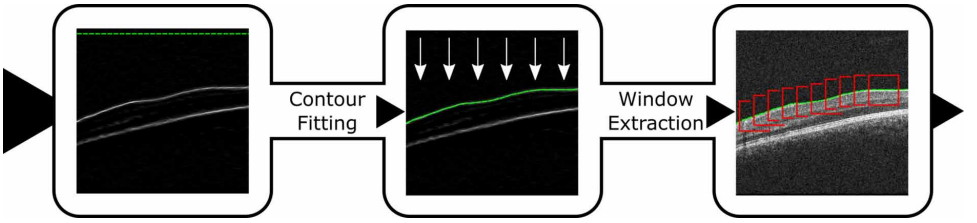

Window Classification

Once the region of interest has been segmented and the windows around each pixel of the ILM have been extracted, the second step is the classification of each of these windows according to whether they are centred around pathological or healthy tissue. The classification of these images can be accomplished by employing a convolutional neural network. These deep learning models can use the convolution operation (Figure 8) in order to make use of the visual information contained in images as features. These models are able to learn a number of convolutional filters that can extract visual features from the images. The progressive stacking of these convolutional filters in depth yields gradually higher-level features. This ability to learn high-level visual representations of information directly from images enables deep learning models to perform a variety of computer vision tasks.

Figure 8. Convolution operation. A convolution filter is applied centred on every image element. The values of the image and the filter are multiplied and gathered in order to obtain the resulting value at each point.

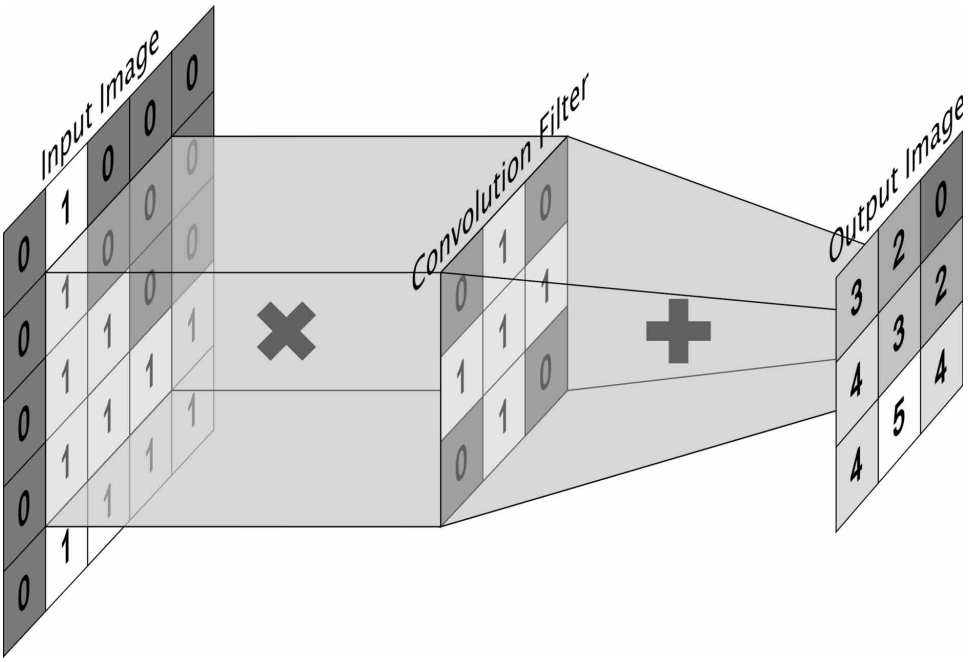

To classify the image windows, Densely Connected Convolutional Neural Networks can be employed (Huang et al., 2017). These deep learning models use dense blocks and the progressive concatenation of lower-level features in order to propagate these further into the architecture. This aids to mitigate the vanishing gradient problem by allowing it to flow directly from the layer closest to the loss to the early ones. This way, the layers close to the original data can be updated more efficiently than in a conventional convolutional neural network. From among the different DenseNet variants, a DenseNet-121 was used for the methodology described in this chapter. A schematic representation of this architecture can be found in Figure 9.

Figure 9. Basic structure of a DenseNet-121 model, detailing the composition of the dense blocks, their dense layers, and the progressive concatenation of visual features

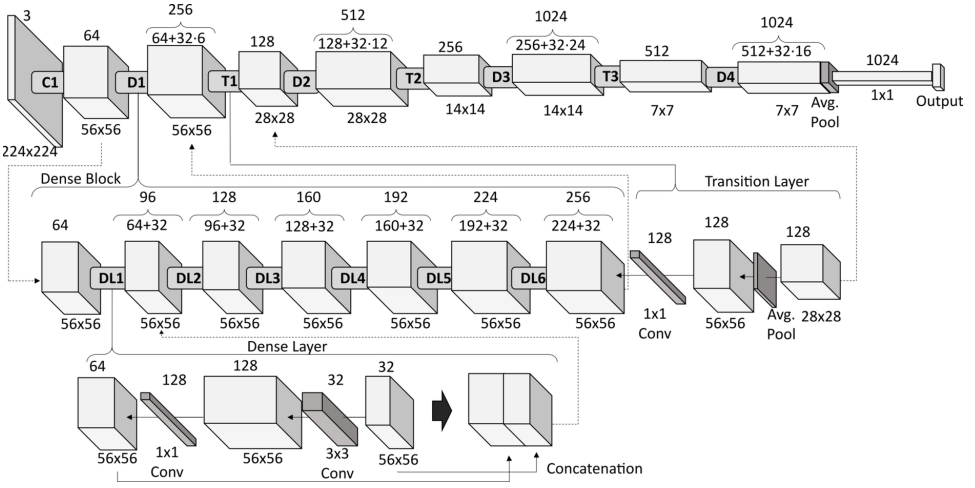

The labels that result from each window classification can be assigned to the original central pixels around which the image windows were extracted. This way, by combining the location of the ILM with its classification into healthy or diseased tissue, a segmentation of the ERM can be effectively produced (Figure 10).

Figure 10. Second step of ERM segmentation. The windows that were extracted in the previous step are classified into healthy or pathological. The resulting labels are assigned to the original pixels around which the windows were extracted.

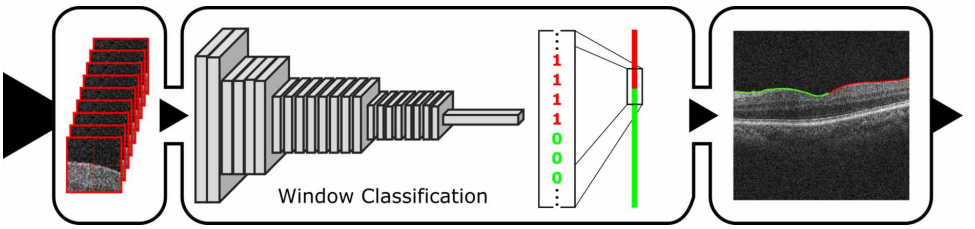

INTUITIVE MAP RECONSTRUCTION

The third and final step is the reconstruction and post-processing of the segmentation maps. In order to provide the experts with an intuitive visualisation of the results, these are reconstructed in the form of a colour map indicating ERM presence or absence overlaid over a representation of the eye fundus. This way, the zone that is

affected by the ERM can be easily interpreted, bypassing the need to observe each of the OCT slices.

For this reconstruction, the information contained in the 3D OCT volumes is leveraged by taking advantage of the consecutive organisation of the 2D OCT slices. These advantages are harnessed in two ways. First, since each OCT tomogram represents a parallel slice of the analysed section of the eye fundus, there is a structural relation between the information contained in consecutive slices. This information can be used to further refine the ERM segmentation by providing a consensus of the classifications of the surrounding boundary points. This way, each image pixel contributes not only to the classification of the spot where it is located and the surrounding pixels in the same slice, but also to the classifications of pixels in the surrounding slices, adding an additional cross-slice dimension through which visual information can be integrated in the segmentation process. This helps to correct spurious misclassifications that may occur due to lighting differences in consecutive slices and softens the segmented boundary region. Second, due to the organisation of the 2D OCT slices, the visual information contained in each of them can be combined in order to recreate a visualisation of the analysed retina section. This visualisation allows for the information contained in the whole cube to be summed up in order to provide a quick analysis and reference of the location of the analysed tissue. This way, the segmentation results and the equivalent location in the eye fundus can be viewed at a glance in the form of colour maps.

To obtain these maps, the one-dimensional classification tag arrays of every slice are laterally stacked together according to their original location. This creates a two-dimensional spatial representation of the classification of every original image column, which can be interpreted as an overview of the eye fundus. In these images, green represents an ILM spot that was classified as healthy, while red represents a diseased one.

Since every image patch was isolated from its context, some outlying pixels classified as ERM can appear. These are mainly caused by a few misclassifications produced by image artefacts and reflections in the original OCT images. In order to correct these, and with the aim to produce a visualisation that better represents the appearance that the ERM has over the eye fundus, a post-processing step is applied. This step incorporates into the classification of every pixel the information contained in the classification of its surrounding neighbours. Additionally, it aims to preserve the softer boundaries that the ERM actually presents.

Figure 11. Third step of ERM segmentation. The 1D classification arrays are converted to colour pixels are stacked in the original order. The resulting segmentation maps are then post-processed in order to filter spurious pixels and produce a regular boundary.

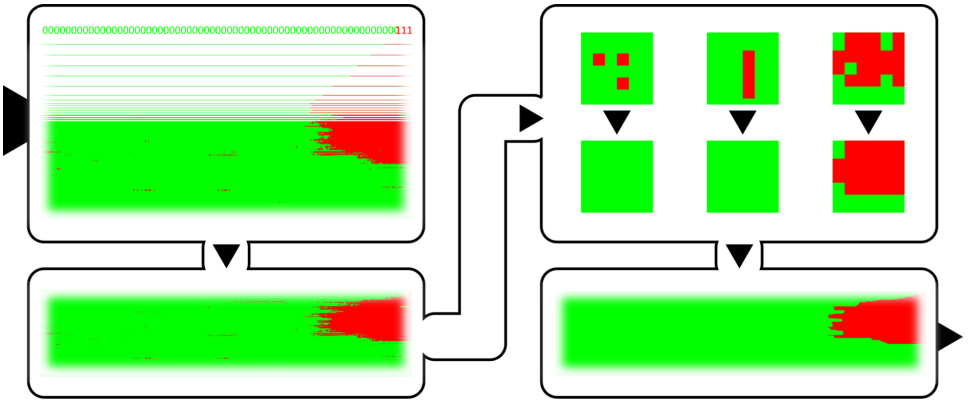

This post-processing step consists of the filtering of any ERM-classified contour under a certain size threshold and morphological filtering. Expert knowledge determines that isolated ERM patches of a very small size are extremely unlikely. Because of this, the first step of this post-processing stage is to filter out any isolated ERM-classified contour under 25 pixels in size. Furthermore, in order to correct spurious misclassifications and preserve the regularity of the boundary region, a morphological opening is performed on the segmentation map using a 10×4 pixel horizontal rectangle as structuring element. This operation is described by Equation 4, where A_b denotes the translation of A by b. Since consecutive OCT slices may show differences in reflectivity, incorporating cross-slice information via this morphological filtering helps preserve boundary regularity. This results in an image where the isolated ERM pixels are filtered out and with a continuous boundary region. The complete reconstruction and the post-processing stage are summed up in Figure 11.

$$\begin{aligned} A \circ B &= \left(A \ominus B\right) \oplus B \\ A \ominus B &= \bigcap_{b \in B} A_{-b} \\ A \oplus B &= \bigcup_{b \in B} A_b \end{aligned} \tag{4}$$

Finally, in order to provide a reference for this map, a representation of the eye fundus is created from the original OCT volume. This representation is created by averaging every image column in the volume. That is, for every slice in the volume, the average value of the pixels in every column is calculated. This value is translated into a pixel brightness value, which can be combined with its neighbours in an orderly manner, in the same way in which the segmentation map is reconstructed. The resulting two-dimensional image shows a representation of the fundus of the eye, allowing a visualisation of the foveal pit, the vascular structure of the eye and any relevant deformations that may be present in the retina (Figure 12). By overlaying the segmentation colour map over the eye fundus reconstruction, the final intuitive visualisation of the ERM is produced.

Figure 12. Reconstruction of the eye fundus representation to be used as reference. The average brightness value of each image column of every OCT slice contained in the original volume is calculated. These values are then combined to produce a 2D image representing the retina of the eye.

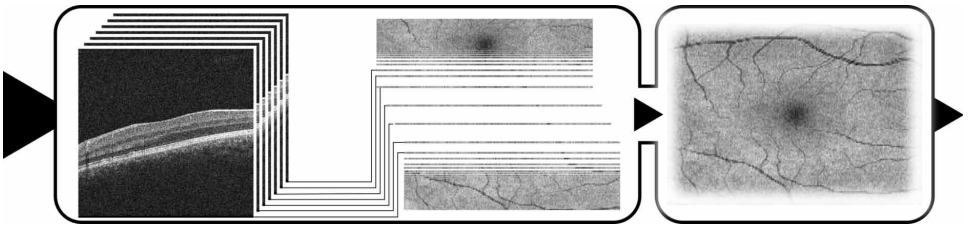

Dataset

The methodology presented in this chapter was comprehensively validated with a representative dataset. Specifically, this dataset consisted of 20 OCT volumes obtained from different patients. Each of these volumes represents an eye. Out of the 20 eyes, 12 belonged to healthy patients, while 8 displayed signs of ERM. These volumes contained a total of 2428 2D OCT slices, with 1,536 belonging to healthy eyes and 892 to eyes with ERM. The platform used to produce these images was a CIRRUS ™ HD-OCT Carl Zeiss Meditec confocal scanning laser ophthalmoscope. These images were obtained in accordance with the Declaration of Helsinki, as approved by the Ethics Committee of Investigation from A Coruña/ Ferrol (2014/437) the 24th of November 2014. All of the images showing ERM signs were manually annotated by an expert indicating the location of the diseased tissue, which served as the dataset ground truth. This dataset was partitioned using a 4-fold cross-validation, with each fold being divided into three sets, using 50% of

the eyes for training, 25% for validation and the remaining 25% for test. In order to preserve a balance between ERM-positive and negative cases, as well as to avoid oversampling the training set, 40 equispaced windows were extracted from every slice belonging to diseased eyes, and 8 from every slice taken from a healthy eye. This resulted in a total of 21,667 pathological samples and 27,536 healthy samples. These were used to train and validate this methodology, ensuring each eye appears in a testing set once.

Training Details

The DenseNet-121 models were trained on the available dataset following the 4-fold cross-validation. This way, 4 models were trained on their corresponding training sets. The training process was allowed to run for a maximum of 100 epochs, selecting the epoch that produced the smallest loss on its corresponding validation set for testing. Cross-entropy loss was used for training, while Adaptive Moment Estimation (Adam) was used for optimisation, with a learning rate of 1×10^{-5}, $\beta1\_0.9$ and $\beta2=_{0}.999$. The 112×112 pixel windows extracted from the images were resized to a standard 224×224 resolution. Furthermore, in order to take a better advantage of the available data, online augmentation was used on the training samples, combining random horizontal flipping, random vertical and horizontal shearing between -15º and 15º as well as random rotation of the windows between -15º and 15º (Figure 13). The borders of the images were reflected with the intention to preserve image continuity after the augmentation.

Figure 13. Example of different augmented variations of the same spot showing signs of ERM

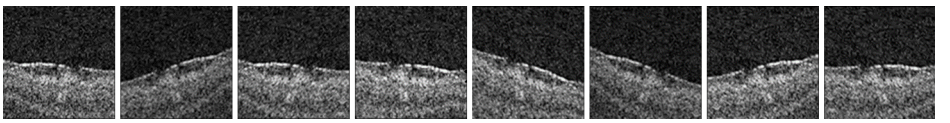

RESULTS AND DISCUSSION

This methodology achieved generally favourable results, both in terms of the classification of image patches and the segmentation of the ERM in the images as a whole. In this sense, this methodology can provide an accurate and robust diagnosis of this pathology. In this section, the results that were obtained by making use of the presented methodology are described and discussed. These results correspond to those produced by the convolutional neural networks when trained and cross-

validated on the previously described dataset. Commonly reported metrics for similar image segmentation tasks such as the Accuracy (Equation 5), Sensitivity or Recall (Equation 6), Specificity (Equation 7), Sørensen-Dice Coefficient (Equation 8) and Jaccard Index (Equation 9) were used.

$$Accuracy = \frac{TP + TN}{TP + TN + FP + FN} \tag{5}$$

$$Sensitivity = Recall = \frac{TP}{TP + FN} \tag{6}$$

$$Specificity = \frac{TN}{TN + FP} \tag{7}$$

$$Dice = \frac{2 \times TP}{2 \times TP + FP + FN} \tag{8}$$

$$Jaccard = \frac{TP}{TP + FP + FN} \tag{9}$$

Figure 14. Accuracy, Precision and Recall of the samples contained in the test sets and by extracting a window around every ILM pixel of the images in this set

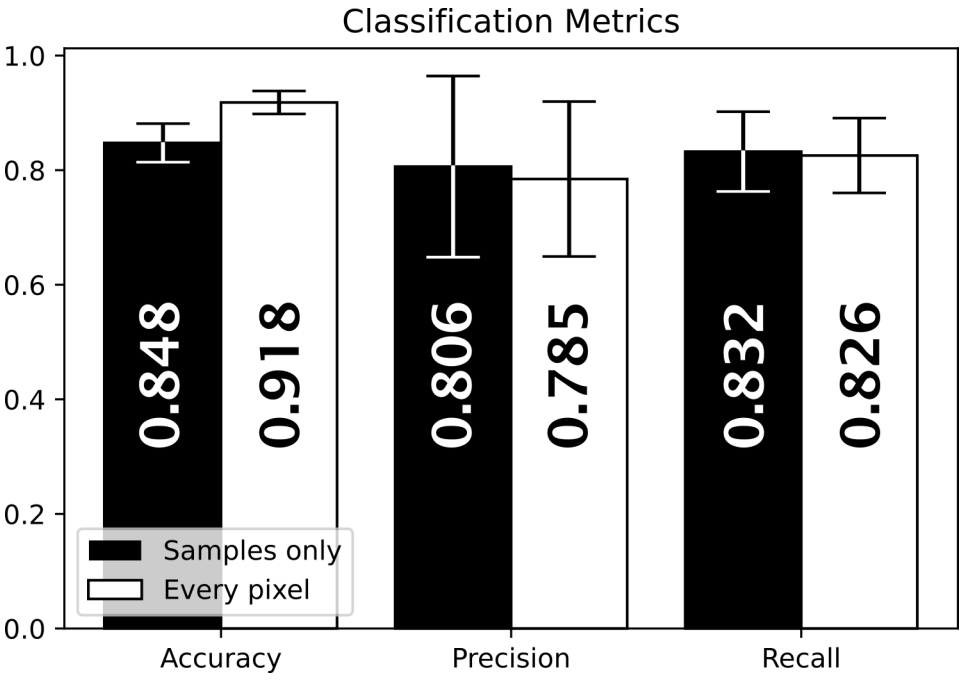

In terms of the classification of the image windows, Figure 14 shows the results that were obtained by every model classifying the window samples contained in the test set. This figure also displays the results obtained from the classification of every window extracted from every pixel contained in the volumes included in the test sets, analogously to how this model would perform when analysing an OCT volume. Respecting the segmentation maps of the ERM, Figure 15 illustrates the Receiver Operating Characteristic as well as the Precision Recall curves described by the models. The Dice Coefficient and the Jaccard Index before and after applying the post-processing stage can be found in Figure 16.

Figure 15. Receiver Operating Characteristic (left) and Precision Recall (right) curves corresponding to the results of the proposed methodology

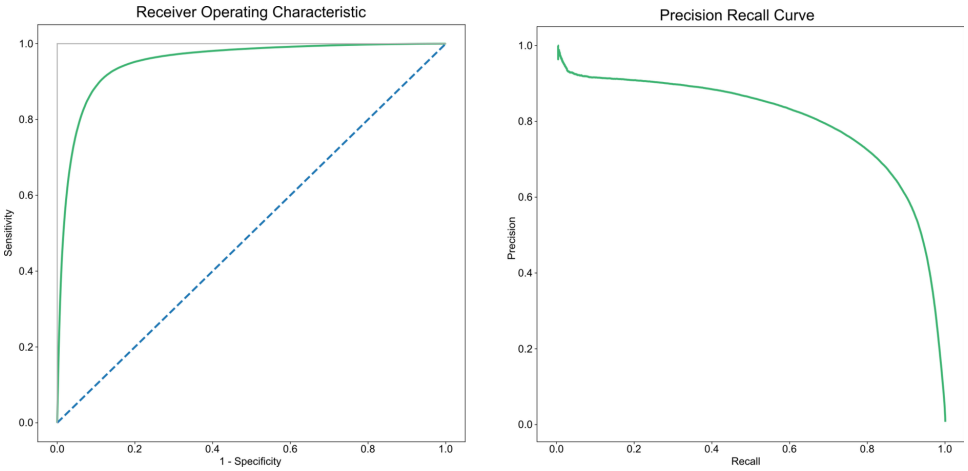

These results show that this methodology can provide a robust and objective segmentation of the ERM in OCT images. By making use of deep learning models, the visual features that are visible at different scales in the images can be used for an accurate characterisation of the ERM. Furthermore, by incorporating the information contained in the surrounding slices into the classification results, these can be refined. Thanks to this post-processing stage, it is possible to achieve better results and provide a segmentation that preserves the actual appearance of the ERM over the eye fundus. The resulting colour maps overlaid over the eye fundus reference have the potential to simplify the analysis process and provide an intuitive diagnosis of this disease.

Figure 16. Dice Coefficient and Jaccard Index corresponding to the segmentation maps before and after the application of the post-processing stage

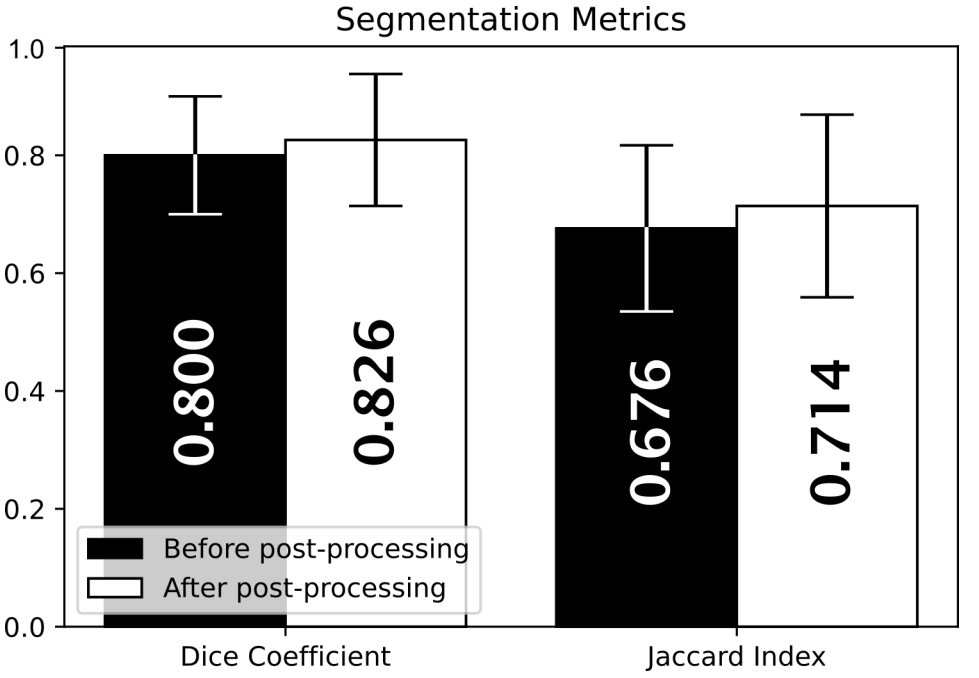

SOLUTIONS AND RECOMMENDATIONS

During the development process of this methodology, the authors identified a number of possible issues and proposed a series of solutions. For the problem of determining the balance between the positive and the negative samples in the dataset, preliminary testing was performed. In this testing, different sampling conditions were compared, with the best results being obtained with the strategy that was described. This strategy consisted in sampling 40 equispaced windows from every image belonging to a pathological eye and 8 from every image in a healthy eye. This relation between samples was chosen in order to preserve a balance between the classes, since the healthy eyes are more numerous and do not contain diseased tissue while the diseased ones are fewer and do contain healthy tissue. Moreover, by using this sampling strategy, there is already a consistent overlap between consecutive windows. Increasing the number of samples extracted from the images further would provide little to no benefit at the risk of overrepresenting the visual information that was already sampled.

The post-processing stage was incorporated to the methodology partially as a solution to the problem of isolated bright pixels caused by image artefacts being

misclassified as ERM-positive spots. Furthermore, there are some differences in lighting and overall image quality between consecutive slices, which can lead to irregular boundary regions when only the information that is contained in a single slice is used to classify ILM pixels. By filtering out the small, isolated spots which are not adjacent to any ERM region and by using morphological filtering to incorporate cross-slice information into the classification of every ILM pixel, these problems can be corrected, resulting in a more uniform segmentation map without isolated ERM-positive pixels and with a more regular boundary between ERM and healthy regions.

FUTURE RESEARCH DIRECTIONS

Future work dedicated to address ERM diagnosis could focus on leveraging the information contained in OCT volumes. This chapter exposed the advantages of combining cross-slice information into the segmentation of each ILM spot. These advantages could be further exploited in the form of three-dimensional analysis by employing 3D convolutional models for the detection of this pathology. This way, the convolutional models can better integrate more of the surrounding slice information into classifying each of the ILM pixels.

Moreover, this methodology could be simplified significantly by training models to perform the automatic segmentation of the ERM tissue. It may be possible to train convolutional neural networks to return segmentation masks directly from the data, bypassing the series of steps described in this chapter and the over reliance on the ILM segmentation pre-processing stage.

Furthermore, the problem of automatically assessing the different stages of ERM and its severity remains to be addressed. By performing a multiclass classification of each segmented ERM pixel into the stages the ERM may present, a more complete evaluation of this relevant eye disease can be produced. In order to achieve many of the tasks that are proposed here, a more comprehensive annotated dataset focused entirely on the segmentation of the ERM may be required.

CONCLUSION

This chapter explores a detailed explanation of a fully automatic methodology for the segmentation of the ERM in OCT images. This methodology takes advantage of computer vision techniques and makes use of state-of-the-art deep learning models in order to provide an accurate and objective detection of the visual features that characterise this disease.

The first step in the proposed methodology is to limit the area that is to be analysed to only that which is susceptible to ERM apparition. To do this, the ILM region is segmented from the images by using active contours. This region is modelled as a height value for every image column, since the ILM appears as a mostly horizontal boundary line in the OCT slices. Due to its horizontality, the ILM region can be highlighted using border detection techniques such as a convolution using the y-axis Sobel operator. The active contour is then allowed to contract downward from the top of the image, eventually converging over the ILM location.

At this point, an image window is extracted around every segmented ILM pixel. These windows are then classified by a DenseNet-121 architecture. This deep learning model returns a label determining whether each image displays healthy or ERM-related tissue. These labels are then assigned to the original ILM pixels, marking whether they should be considered healthy or diseased tissue. This way, an effective segmentation of the ERM can be produced by means of a classification of windows.

The arrays containing the labels of each OCT slice segmentation are then combined with those of the consecutive slices. This produces a two-dimensional segmentation map which shows the ERM presence in an overhead view. In order to further refine these maps, a post-processing stage based on expert clinical knowledge is applied. After this post-processing stage, the maps display a uniform ERM region, according to its real appearance. This post-processing stage also contributes to improve the results, since it filters out many misclassifications that may occur due to image artefacts.

Finally, an overhead visualisation of the eye fundus is generated based on the original OCT volume. This visualisation is synthesised by calculating the average brightness value of every image column in the set. This visualisation clearly displays the foveal pit as well as the vascular structure of the retina and any irregularities that may be present. This representation serves as a reference with which to interpret the ERM segmentation maps. As a final step, these two images are overlaid in order to present the segmentation results in an intuitive and simple manner, helping provide robustness and objectivity to the diagnosis of this relevant pathology.

ACKNOWLEDGMENT

This research was funded by Instituto de Salud Carlos III, Government of Spain, [research project DTS18/00136]; Ministerio de Ciencia e Innovación y Universidades, Government of Spain, [research project RTI2018-095894-B-I00]; Ministerio de Ciencia e Innovación, Government of Spain [research project PID2019-108435RB-I00]; Consellería de Cultura, Educación e Universidade, Xunta de Galicia, Grupos de Referencia Competitiva, [grant ref. ED431C 2020/24], predoctoral [grant ref. ED481A 2021/161] and postdoctoral [grant ref. ED481B

2021/059]; Axencia Galega de Innovación (GAIN), Xunta de Galicia, [grant ref. IN845D 2020/38]; CITIC, Centro de Investigación de Galicia [grant ref. ED431G 2019/01], receives financial support from Consellería de Educación, Universidade e Formación Profesional, Xunta de Galicia, through the ERDF (80%) and Secretaría Xeral de Universidades (20%).

REFERENCES

Baamonde, S., de Moura, J., Novo, J., Charlón, P., & Ortega, M. (2019a). Automatic identification and characterization of the epiretinal membrane in OCT images. *Biomedical Optics Express*, *10*(8), 4018. doi:10.1364/BOE.10.004018 PMID:31452992

Baamonde, S., de Moura, J., Novo, J., Charlón, P., & Ortega, M. (2019b). Automatic Identification and Intuitive Map Representation of the Epiretinal Membrane Presence in 3D OCT Volumes. *Sensors (Basel)*, *19*(23), 5269. doi:10.339019235269 PMID:31795480

Baamonde, S., de Moura, J., Novo, J., & Ortega, M. (2017a). Automatic Detection of Epiretinal Membrane in OCT Images by Means of Local Luminosity Patterns. In I. Rojas, G. Joya, & A. Catala (Eds.), *Advances in Computational Intelligence* (pp. 222–235). Springer International Publishing. doi:10.1007/978-3-319-59153-7_20

Baamonde, S., de Moura, J., Novo, J., Rouco, J., & Ortega, M. (2017b). Feature Definition and Selection for Epiretinal Membrane Characterization in Optical Coherence Tomography Images. In *Image Analysis and Processing - ICIAP 2017* (pp. 456–466). Springer International Publishing. doi:10.1007/978-3-319-68548-9_42

Borrelli, E., Sarraf, D., Freund, K. B., & Sadda, S. R. (2018, November). OCT angiography and evaluation of the choroid and choroidal vascular disorders. *Progress in Retinal and Eye Research*, *67*, 30–55. doi:10.1016/j.preteyeres.2018.07.002 PMID:30059755

Cheng, J.-Z., Ni, D., Chou, Y.-H., Qin, J., Tiu, C.-M., Chang, Y.-C., Huang, C.-S., Shen, D., & Chen, C.-M. (2016, April). Computer-Aided Diagnosis with Deep Learning Architecture: Applications to Breast Lesions in US Images and Pulmonary Nodules in CT Scans. *Scientific Reports*, *6*(1), 24454. Advance online publication. doi:10.1038rep24454 PMID:27079888

de Moura, J., Novo, J., & Ortega, M. (2019). Deep Feature Analysis in a Transfer Learning-based Approach for the Automatic Identification of Diabetic Macular Edema. In *2019 International Joint Conference on Neural Networks (IJCNN)* (pp. 1-8). Institute of Electrical and Electronics Engineer. 10.1109/IJCNN.2019.8852196

de Moura, J., Novo, J., Ortega, M., & Charlón, P. (2016). 3D retinal vessel tree segmentation and reconstruction with OCT images. In *Image Analysis and Recognition* (pp. 716–726). Lecture Notes in Computer Science. Springer. doi:10.1007/978-3-319-41501-7_80

de Moura, J., Novo, J., Rouco, J., Penedo, M. G., & Ortega, M. (2017). *Automatic detection of blood vessels in retinal OCT images*. International Work-Conference on the Interplay Between Natural and Artificial Computation. doi:10.1007/978-3-319-59773-7_1

de Moura, J., Samagaio, G., Novo, J., Almuina, P., Fernández, M. I., & Ortega, M. (2020, June). Joint Diabetic Macular Edema Segmentation and Characterization in OCT Images. *Journal of Digital Imaging*, *33*(5), 1335–1351. doi:10.100710278-020-00360-y PMID:32562127

de Moura, J., Vidal, P. L., Novo, J., Rouco, J., & Ortega, M. (2017). Feature definition, analysis and selection for cystoid region characterization in Optical Coherence Tomography. In *Knowledge-Based and Intelligent Information & Engineering Systems: Proceedings of the 21st International Conference* (pp. 1369-1377). Elsevier. 10.1016/j.procs.2017.08.043

Doi, K. (2007, June). Computer-aided diagnosis in medical imaging: Historical review, current status and future potential. *Computerized Medical Imaging and Graphics*, *31*(4-5), 198–211. doi:10.1016/j.compmedimag.2007.02.002 PMID:17349778

Fang, L., Yang, L., Li, S., Rabbani, H., Liu, Z., Peng, Q., & Chen, X. (2017, June). Automatic detection and recognition of multiple macular lesions in retinal optical coherence tomography images with multi-instance multilabel learning. *Journal of Biomedical Optics*, *22*(6), 066014. doi:10.1117/1.JBO.22.6.066014 PMID:28655052

Fernández, A., Ortega, M., de Moura, J., Novo, J., & Penedo, M. G. (2018, June). Detection of reactions to sound via gaze and global eye motion analysis using camera streaming. *Machine Vision and Applications*, *29*(7), 1069–1082. doi:10.100700138-018-0952-9

Gawlik, K., Hausser, F., Paul, F., Brandt, A. U., & Kadas, E. M. (2018, December). Active contour method for ILM segmentation in ONH volume scans in retinal OCT. *Biomedical Optics Express*, *9*(12), 6497–6518. doi:10.1364/BOE.9.006497 PMID:31065445

Gende, M., Moura, J. D., Novo, J., Charlon, P., & Ortega, M. (2021). Automatic Segmentation and Intuitive Visualisation of the Epiretinal Membrane in 3D OCT Images Using Deep Convolutional Approaches. *IEEE Access: Practical Innovations, Open Solutions*, *9*, 75993–76004. doi:10.1109/ACCESS.2021.3082638

Ghazi, N. G., Ciralsky, J. B., Shah, S. M., Campochiaro, P. A., & Haller, J. A. (2007). Optical coherence tomography findings in persistent diabetic macular edema: The vitreomacular interface. *American Journal of Ophthalmology*, *144*(5), 747–754. doi:10.1016/j.ajo.2007.07.012 PMID:17869207

Gulshan, V., Peng, L., Coram, M., Stumpe, M. C., Wu, D., Narayanaswamy, A., Venugopalan, S., Widner, K., Madams, T., Cuadros, J., Kim, R., Raman, R., Nelson, P. C., Mega, J. L., & Webster, D. R. (2016, December). Development and Validation of a Deep Learning Algorithm for Detection of Diabetic Retinopathy in Retinal Fundus Photographs. *Journal of the American Medical Association*, *316*(22), 2402. doi:10.1001/jama.2016.17216 PMID:27898976

Hee, M. R. (1995, August). Quantitative Assessment of Macular Edema With Optical Coherence Tomography. *Archives of Ophthalmology*, *113*(8), 1019. doi:10.1001/archopht.1995.01100080071031 PMID:7639652

Hood, D. C. (2017, March). Improving our understanding, and detection, of glaucomatous damage: An approach based upon optical coherence tomography (OCT). *Progress in Retinal and Eye Research*, *57*, 46–75. doi:10.1016/j.preteyeres.2016.12.002 PMID:28012881

Hosny, A., Parmar, C., Quackenbush, J., Schwartz, L. H., & Aerts, H. J. (2018, May). Artificial intelligence in radiology. *Nature Reviews. Cancer*, *18*(8), 500–510. doi:10.103841568-018-0016-5 PMID:29777175

Huang, D., Swanson, E. A., Lin, C. P., Schuman, J. S., Stinson, W. G., Chang, W., Hee, M. R., Flotte, T., Gregory, K., Puliafito, C. A., & Fujimoto, J. G. (1991). Optical Coherence Tomography. *Science*, *254*(5035), 1178–1181. doi:10.1126cience.1957169 PMID:1957169

Huang, G., Liu, Z., Van Der Maaten, L., & Weinberger, K. Q. (2017). Densely Connected Convolutional Networks. *2017 IEEE Conference on Computer Vision and Pattern Recognition (CVPR)*, 2261-2269. 10.1109/CVPR.2017.243

Jaffe, G. J., & Caprioli, J. (2004, January). Optical coherence tomography to detect and manage retinal disease and glaucoma. *American Journal of Ophthalmology*, *137*(1), 156–169. doi:10.1016/S0002-9394(03)00792-X PMID:14700659

Kamnitsas, K., Ledig, C., Newcombe, V. F., Simpson, J. P., Kane, A. D., Menon, D. K., Rueckert, D., & Glocker, B. (2017, February). Efficient multi-scale 3D CNN with fully connected CRF for accurate brain lesion segmentation. *Medical Image Analysis*, *36*, 61–78. doi:10.1016/j.media.2016.10.004 PMID:27865153

Kanopoulos, N., Vasanthavada, N., & Baker, R. L. (1988). Design of an image edge detection filter using the Sobel operator. *IEEE Journal of Solid-State Circuits*, *23*(2), 358–367. doi:10.1109/4.996

Kashani, A. H., Chen, C.-L., Gahm, J. K., Zheng, F., Richter, G. M., Rosenfeld, P. J., Shi, Y., & Wang, R. K. (2017, September). Optical coherence tomography angiography: A comprehensive review of current methods and clinical applications. *Progress in Retinal and Eye Research*, *60*, 66–100. doi:10.1016/j.preteyeres.2017.07.002 PMID:28760677

Kass, M., Witkin, A., & Terzopoulos, D. (1988, January). Snakes: Active contour models. *International Journal of Computer Vision*, *1*(4), 321–331. doi:10.1007/BF00133570

Kim, J., Hong, J., & Park, H. (2018, June). Prospects of deep learning for medical imaging. *Precision and Future Medicine*, *2*(2), 37–52. doi:10.23838/pfm.2018.00030

Kingma, D. P., & Ba, J. (2015). Adam: A Method for Stochastic Optimization. In Y. Bengio, & Y. LeCun (Ed.), *3rd International Conference on Learning Representations, ICLR 2015*, *San Diego, CA, USA*, *May 7-9, 2015*, *Conference Track Proceedings.* Retrieved from https://arxiv.org/abs/1412.6980

Krizhevsky, A., Sutskever, I., & Hinton, G. E. (2017, May). ImageNet classification with deep convolutional neural networks. *Communications of the ACM*, *60*(6), 84–90. doi:10.1145/3065386

Kuwayama, S., Ayatsuka, Y., Yanagisono, D., Uta, T., Usui, H., Kato, A., Takase, N., Ogura, Y., & Yasukawa, T. (2019, April). Automated Detection of Macular Diseases by Optical Coherence Tomography and Artificial Intelligence Machine Learning of Optical Coherence Tomography Images. *Journal of Ophthalmology*, *2019*, 1–7. doi:10.1155/2019/6319581 PMID:31093370

Lakhani, P., & Sundaram, B. (2017, August). Deep Learning at Chest Radiography: Automated Classification of Pulmonary Tuberculosis by Using Convolutional Neural Networks. *Radiology*, *284*(2), 574–582. doi:10.1148/radiol.2017162326 PMID:28436741

LeCun, Y., Bengio, Y., & Hinton, G. (2015, May). Deep learning. *Nature*, *521*(7553), 436–444. doi:10.1038/nature14539 PMID:26017442

Lecun, Y., Bottou, L., Bengio, Y., & Haffner, P. (1998). Gradient-based learning applied to document recognition. *Proceedings of the IEEE*, *86*(11), 2278–2324. doi:10.1109/5.726791

Lee, J.-H., Kim, Y.-T., Lee, J.-B., & Jeong, S.-N. (2020, November). A Performance Comparison between Automated Deep Learning and Dental Professionals in Classification of Dental Implant Systems from Dental Imaging: A Multi-Center Study. *Diagnostics (Basel)*, *10*(11), 910. doi:10.3390/diagnostics10110910 PMID:33171758

Litjens, G., Kooi, T., Bejnordi, B. E., Setio, A. A., Ciompi, F., Ghafoorian, M., van der Laak, J. A. W. M., van Ginneken, B., & Sánchez, C. I. (2017, December). A survey on deep learning in medical image analysis. *Medical Image Analysis*, *42*, 60–88. doi:10.1016/j.media.2017.07.005 PMID:28778026

Lo, Y.-C., Lin, K.-H., Bair, H., Sheu, W. H.-H., Chang, C.-S., Shen, Y.-C., & Hung, C.-L. (2020, May). Epiretinal Membrane Detection at the Ophthalmologist Level using Deep Learning of Optical Coherence Tomography. *Scientific Reports*, *10*(1), 8424. Advance online publication. doi:10.103841598-020-65405-2 PMID:32439844

Long, J., Shelhamer, E., & Darrell, T. (2015, June). Fully convolutional networks for semantic segmentation. In *2015 IEEE Conference on Computer Vision and Pattern Recognition*. IEEE. 10.1109/CVPR.2015.7298965

Lu, W., Tong, Y., Yu, Y., Xing, Y., Chen, C., & Shen, Y. (2018, December). Deep Learning-Based Automated Classification of Multi-Categorical Abnormalities From Optical Coherence Tomography Images. *Translational Vision Science & Technology*, *7*(6), 41. doi:10.1167/tvst.7.6.41 PMID:30619661

Lv, Y., Duan, Y., Kang, W., Li, Z., & Wang, F.-Y. (2014). Traffic Flow Prediction With Big Data: A Deep Learning Approach. *IEEE Transactions on Intelligent Transportation Systems*, 1–9. doi:10.1109/TITS.2014.2345663

Massin, P., Allouch, C., Haouchine, B., Metge, F., Paques, M., Tangui, L., Erginay, A., & Gaudric, A. (2000, December). Optical coherence tomography of idiopathic macular epiretinal membranes before and after surgery. *American Journal of Ophthalmology*, *130*(6), 732–739. doi:10.1016/S0002-9394(00)00574-2 PMID:11124291

Matsumoto, C., Arimura, E., Okuyama, S., Takada, S., Hashimoto, S., & Shimomura, Y. (2003, September). Quantification of Metamorphopsia in Patients with Epiretinal Membranes. *Investigative Ophthalmology & Visual Science*, *44*(9), 4012. doi:10.1167/iovs.03-0117 PMID:12939323

Mitchell, P., Liew, G., Gopinath, B., & Wong, T. Y. (2018, September). Age-related macular degeneration. *Lancet*, *392*(10153), 1147–1159. doi:10.1016/S0140-6736(18)31550-2 PMID:30303083

Mookiah, M. R., Acharya, U. R., Chua, C. K., Lim, C. M., Ng, E. Y., & Laude, A. (2013, December). Computer-aided diagnosis of diabetic retinopathy: A review. *Computers in Biology and Medicine*, *43*(12), 2136–2155. doi:10.1016/j.compbiomed.2013.10.007 PMID:24290931

Parra-Mora, E., Cazañas-Gordon, A., Proença, R., & da Silva Cruz, L. A. (2021). Epiretinal Membrane Detection in Optical Coherence Tomography Retinal Images Using Deep Learning. *IEEE Access: Practical Innovations, Open Solutions*, *9*, 99201–99219. doi:10.1109/ACCESS.2021.3095655

Rahman, R., & Stephenson, J. (2014, January). Early surgery for epiretinal membrane preserves more vision for patients. *Eye (London, England)*, *28*(4), 410–414. doi:10.1038/eye.2013.305 PMID:24406414

Romeny, B. M., Zuiderveld, K. J., Waes, P. F., Walsum, T. V., Weijden, R. V., Weickert, J., ... Viergever, M. A. (1998, October). Advances in three-dimensional diagnostic radiology. *Journal of Anatomy*, *193*(3), 363–371. doi:10.1046/j.1469-7580.1998.19330363.x PMID:9877291

Samagaio, G., de Moura, J., Novo, J., & Ortega, M. (2017). Optical Coherence Tomography Denoising by Means of a Fourier Butterworth Filter-based Approach. In *Image Analysis and Processing - ICIAP 2017* (pp. 422–432). Lecture Notes in Computer Science. Springer. doi:10.1007/978-3-319-68548-9_39

Setio, A. A., Ciompi, F., Litjens, G., Gerke, P., Jacobs, C., van Riel, S. J., Wille, M. M. W., Naqibullah, M., Sanchez, C. I., & van Ginneken, B. (2016, May). Pulmonary Nodule Detection in CT Images: False Positive Reduction Using Multi-View Convolutional Networks. *IEEE Transactions on Medical Imaging*, *35*(5), 1160–1169. doi:10.1109/TMI.2016.2536809 PMID:26955024

Shen, D., Wu, G., & Suk, H.-I. (2017, June). Deep Learning in Medical Image Analysis. *Annual Review of Biomedical Engineering*, *19*(1), 221–248. doi:10.1146/annurev-bioeng-071516-044442 PMID:28301734

Sonobe, T., Tabuchi, H., Ohsugi, H., Masumoto, H., Ishitobi, N., Morita, S., Enno, H., & Nagasato, D. (2018, September). Comparison between support vector machine and deep learning, machine-learning technologies for detecting epiretinal membrane using 3D-OCT. *International Ophthalmology*, *39*(8), 1871–1877. doi:10.100710792-018-1016-x PMID:30218173

Spaide, R. F., Fujimoto, J. G., Waheed, N. K., Sadda, S. R., & Staurenghi, G. (2018, May). Optical coherence tomography angiography. *Progress in Retinal and Eye Research*, *64*, 1–55. doi:10.1016/j.preteyeres.2017.11.003 PMID:29229445

Suh, M. H., Seo, J. M., Park, K. H., & Yu, H. G. (2009, March). Associations Between Macular Findings by Optical Coherence Tomography and Visual Outcomes After Epiretinal Membrane Removal. *American Journal of Ophthalmology*, *147*(3), 473–480.e3. doi:10.1016/j.ajo.2008.09.020 PMID:19054492

Tan, O., Chopra, V., Lu, A. T.-H., Schuman, J. S., Ishikawa, H., Wollstein, G., Varma, R., & Huang, D. (2009, December). Detection of Macular Ganglion Cell Loss in Glaucoma by Fourier-Domain Optical Coherence Tomography. *Ophthalmology*, *116*(12), 2305–2314.e2. doi:10.1016/j.ophtha.2009.05.025 PMID:19744726

Ting, D. S., Cheung, C. Y.-L., Lim, G., Tan, G. S., Quang, N. D., Gan, A., Hamzah, H., Garcia-Franco, R., San Yeo, I. Y., Lee, S. Y., Wong, E. Y. M., Sabanayagam, C., Baskaran, M., Ibrahim, F., Tan, N. C., Finkelstein, E. A., Lamoureux, E. L., Wong, I. Y., Bressler, N. M., ... Wong, T. Y. (2017, December). Development and Validation of a Deep Learning System for Diabetic Retinopathy and Related Eye Diseases Using Retinal Images From Multiethnic Populations With Diabetes. *Journal of the American Medical Association*, *318*(22), 2211. doi:10.1001/jama.2017.18152 PMID:29234807

Vidal, P. L., de Moura, J., Novo, J., Penedo, M. G., & Ortega, M. (2018, September). Intraretinal fluid identification via enhanced maps using optical coherence tomography images. *Biomedical Optics Express*, *9*(10), 4730. doi:10.1364/BOE.9.004730 PMID:30319899

Wilkins, J. R., Puliafito, C. A., Hee, M. R., Duker, J. S., Reichel, E., Coker, J. G., Schuman, J. S., Swanson, E. A., & Fujimoto, J. G. (1996, December). Characterization of Epiretinal Membranes Using Optical Coherence Tomography. *Ophthalmology*, *103*(12), 2142–2151. doi:10.1016/S0161-6420(96)30377-1 PMID:9003350

Yamamoto, T., Akabane, N., & Takeuchi, S. (2001). Vitrectomy for diabetic macular edema: The role of posterior vitreous detachment and epimacular membrane. *American Journal of Ophthalmology*, *132*(3), 369–377. doi:10.1016/S0002-9394(01)01050-9 PMID:11530050

ADDITIONAL READING

Bowling, B. (2015). *Kanski's clinical ophthalmology* (8th ed.). W B Saunders.

De Fauw, J., Ledsam, J. R., Romera-Paredes, B., Nikolov, S., Tomasev, N., Blackwell, S., Askham, H., Glorot, X., O'Donoghue, B., Visentin, D., van den Driessche, G., Lakshminarayanan, B., Meyer, C., Mackinder, F., Bouton, S., Ayoub, K., Chopra, R., King, D., Karthikesalingam, A., ... Ronneberger, O. (2018). Clinically applicable deep learning for diagnosis and referral in retinal disease. *Nature Medicine*, *24*(9), 1342–1350. doi:10.103841591-018-0107-6 PMID:30104768

Doi, K. (2007, June). Computer-aided diagnosis in medical imaging: Historical review, current status and future potential. *Computerized Medical Imaging and Graphics*, *31*(4-5), 198–211. doi:10.1016/j.compmedimag.2007.02.002 PMID:17349778

Gende, M., de Moura, J. D., Novo, J., Charlón, P., & Ortega, M. (2021). Automatic segmentation and intuitive visualisation of the epiretinal membrane in 3D OCT images using deep convolutional approaches. *IEEE Access: Practical Innovations, Open Solutions*, *24*, 75993–76004. doi:10.1109/ACCESS.2021.3082638

Keane, P. A., Patel, P. J., Liakopoulos, S., Heussen, F. M., Sadda, S. R., & Tufail, A. (2012). Evaluation of age-related macular degeneration with optical coherence tomography. *Survey of Ophthalmology*, *57*(5), 389–414. doi:10.1016/j.survophthal.2012.01.006 PMID:22898648

LeCun, Y., Bengio, Y., & Hinton, G. (2015, May). Deep learning. *Nature*, *521*(7553), 436–444. doi:10.1038/nature14539 PMID:26017442

Schmidt-Erfurth, U., Sadeghipour, A., Gerendas, B. S., Waldstein, S. M., & Bogunović, H. (2018). Artificial intelligence in retina. *Progress in Retinal and Eye Research*, *67*, 1–29. doi:10.1016/j.preteyeres.2018.07.004 PMID:30076935

Vidal, P. L., de Moura, J., Novo, J., Penedo, M. G., & Ortega, M. (2018, September). Intraretinal fluid identification via enhanced maps using optical coherence tomography images. *Biomedical Optics Express*, *9*(10), 4730. doi:10.1364/BOE.9.004730 PMID:30319899

KEY TERMS AND DEFINITIONS

Artificial Neural Network: Computing system inspired by neurons which can learn to convert a series of input features into a meaningful output.

Epiretinal Membrane (ERM): Thin fibrocellular layer that may appear over the eye macula idiopathically or as a secondary factor of other pathologies. May cause irreversible visual distortions.

Fovea: Central pit in the middle of the macula of the retina. Composed of closely packed cones, it is responsible for approximately half of the visual information produced by the whole retina.

Inner Limiting Membrane (ILM): Layer that serves as a boundary between the vitreous body and the retina. It is the layer over which the ERM may appear.

Macula: Pigmented area near the centre of the ocular retina that is responsible for the acute, high-resolution colour vision.

Optical Coherence Tomography (OCT): Medical imaging technique that uses low coherence light to produce cross-sectional visualisations of tissue. It can produce volumes that display the tissue of the patient in three dimensions.

Retina: Light-sensitive layer of tissue located at the back of the eye. It is responsible for the translation of light into electrical neural impulses that can be interpreted by the brain.

Segmentation: In computer vision, the process of partitioning an image into multiple zones, areas, or segments, according to their content.